Effects of composition and pressure on

² electronic states of iron in bridgmanite

- 3 Susannah M. Dorfman^{1,2}, Vasily Potapkin³, Mingda Lv¹, Eran Greenberg^{4,*}, Ilya Kupenko^{3,5},
- 4 Aleksandr I. Chumakov⁵, Wenli Bi^{6,7}, E. Ercan Alp⁶, Jiachao Liu¹, Arnaud Magrez⁸, Siân E.
- 5 Dutton^{9,†}, Robert J. Cava⁹, Catherine A. McCammon¹⁰, Philippe Gillet²
- 6 1: Department of Earth and Environmental Sciences, Michigan State University, East Lansing,
- 7 MI, USA.
- 8 2: Earth and Planetary Science Laboratory, Institute of Physics, École Polytechnique Fédérale de
- 9 Lausanne, CH-1015 Lausanne, Switzerland.
- 10 3: Institute of Mineralogy, University of Münster, Münster, Germany.
- 4: School of Physics & Astronomy, Tel-Aviv University, Tel-Aviv, Israel.
- 12 5: ESRF-The European Synchrotron, 71, Avenue des Martyrs, Grenoble, France.
- 6: Advanced Photon Source, Argonne National Laboratory, Argonne, Illinois 60439, USA.
- 7: Department of Geology, University of Illinois at Urbana-Champaign, Urbana, Illinois 61801.
- USA; Department of Physics, University of Alabama at Birmingham, Birmingham, Alabama
- 16 35294, USA.
- 8: Crystal Growth Facility, Institute of Physics, École Polytechnique Fédérale de Lausanne, CH-
- 18 1015 Lausanne, Switzerland.

- 19 9: Department of Chemistry, Princeton University, Princeton, NJ, USA.
- 20 10: Bayerisches Geoinstitut, University of Bayreuth, Bayreuth, Germany.
- *now at Applied Physics Department, Soreq Nuclear Research Center (NRC), Yavne 81800,
- 22 Israel.

24

[†]now at Cavendish Laboratory, University of Cambridge, Cambridge, CB3 OHE, UK.

Abstract

25 Electronic states of iron in the lower mantle's dominant mineral, (Mg,Fe,Al)(Fe,Al,Si)O₃ bridgmanite, control physical properties of the mantle including density, elasticity, and electrical 26 27 and thermal conductivity. However, determination of electronic states of iron has been 28 controversial, in part due to different interpretations of Mössbauer spectroscopy results used to 29 identify spin state, valence state, and site occupancy of iron. We applied energy-domain 30 Mössbauer spectroscopy to a set of four bridgmanite samples spanning a wide range of compositions: 10-50% Fe/total cations, 0-25% Al/total cations, 12-100% Fe³⁺/total Fe. 31 Measurements performed in the diamond anvil cell at pressures up to 76 GPa below and above 32 the high to low spin transition in Fe³⁺ provide a Mössbauer reference library for bridgmanite and 33 34 demonstrate the effects of pressure and composition on electronic states of iron. Results indicate that although the spin transition in Fe³⁺ in the bridgmanite B-site occurs as predicted, it does not 35

strongly affect the observed quadrupole splitting of 1.4 mm/s, and only decreases center shift for

this site to 0 mm/s at \sim 70 GPa. Thus center shift can easily distinguish Fe³⁺ from Fe²⁺ at high

pressure, which exhibits two distinct Mössbauer sites with center shift ~1 mm/s and quadrupole

splitting 2.4-3.1 and 3.9 mm/s at \sim 70 GPa. Correct quantification of Fe³⁺/total Fe in bridgmanite

2

36

37

38

- is required to constrain effects of composition and redox states in experimental measurements of seismic properties of bridgmanite. In Fe-rich, mixed-valence bridgmanite at deep-mantle-relevant pressures, up to ~20% of the Fe may be a Fe^{2.5+} charge transfer component, which should enhance electrical and thermal conductivity in Fe-rich heterogeneities at the base of Earth's mantle.
- Keywords: bridgmanite, Mössbauer spectroscopy, iron oxidation state, lower mantle

Introduction

Iron-bearing bridgmanite, the most abundant material in the Earth's interior, is the dominant mineral responsible for chemical and physical behavior of the lower mantle. Redox of iron in bridgmanite buffers the mantle and thus has implications for formation of the atmosphere and habitability of the planet, storage and transport of volatiles including water and carbon in the deep interior, and interpretation of structures and dynamic processes observed by seismic tomography (e.g. Frost and McCammon 2008; Gu et al. 2016; Liu et al. 2018). Heterogeneous structures at the base of the mantle including large low shear velocity provinces and ultra-low velocity zones have been suggested to be iron-rich relative to surrounding mantle based on inversion of normal mode data (Ishii and Tromp 1999), tidal tomography (Lau et al. 2017), and travel times of seismic waves reflected off the core-mantle boundary (Rost et al. 2005); identifying these features and their role in the differentiation and mixing of the mantle depends on accurate constraints on the physical properties of iron-rich bridgmanite. Because bridgmanite samples from the lower mantle have not been recovered, redox conditions are inferred based on

60 remote geophysical observations and experimental and theoretical modeling of chemistry at 61 extreme pressures and temperatures. 62 Depth and composition both affect redox states of iron incorporated in the mantle's dominant phase, but efforts to measure these changes have been complicated by the crystal chemistry of 63 64 (Mg,Fe,Al)(Fe,Al,Si)O₃ bridgmanite (e.g. McCammon et al. 2013; Shim et al. 2017). 65 Bridgmanite adopts the orthorhombic GdFeO₃-type perovskite structure, with a larger 8-12-fold pseudo-dodecahedral "A" site and smaller 6-fold octahedral "B" site. Both Fe²⁺ and Fe³⁺ 66 substitute for Mg in the A-site, while only the smaller Fe³⁺ ion may substitute for Si in the B-site. 67 68 At pressure/temperature conditions corresponding to the top of the lower mantle, bridgmanite typically exhibits Fe³⁺/total Fe ratio at least 50%, even under reducing conditions in contact with 69 metallic iron (Frost et al. 2004; Shim et al. 2017). The Fe³⁺/total Fe ratio in bridgmanite 70 71 synthesized at pressures corresponding to the deep lower mantle has been observed to decrease 72 with pressure to $\sim 15\%$, then increase again to $\sim 50\%$ (Shim et al. 2017). Variations in valence states of iron with depth are inferred to be due to energetics of substitution mechanisms as local 73 74 structure and spin state of iron change with depth. Distortion of the perovskite structure due to 75 pressure and/or composition divides the A-site into A1- and A2-sites (Hsu et al. 2010; Hummer and Fei 2012) and occurs at similar conditions as the observed decrease in Fe³⁺/total Fe. A spin-76 77 pairing transition in Fe³⁺ in the B-site at ~48 GPa, corresponding to the mid-lower-mantle, may also drive partitioning of Fe³⁺ into the B-site (Badro et al. 2004; Catalli et al. 2010, 2011; Hsu et 78 al. 2011; Liu et al. 2018). The presence of Al may also modify incorporation of Fe³⁺ in 79 80 bridgmanite through paired substitution of trivalent cations for Mg and Si (e.g. Frost and 81 Langenhorst 2002; Piet et al. 2016) and formation of vacancies in cation (Sinmyo et al. 2014;

82	Kupenko et al. 2015) or oxygen sites (Grüninger et al. 2019; Liu et al. 2019). Based on
83	experiments (e.g. Potapkin et al. 2013) and computational modeling using density functional
84	theory (DFT) (Caracas 2010), paired substitution places Al in the B-site and Fe ³⁺ in the A-site at
85	equilibrium, though some observations support migration of Al and Fe ³⁺ between the two sites
86	(Catalli et al. 2011) and/or migration of Fe ³⁺ from A to B site due to vacancy redistribution
87	(Kupenko et al. 2015). In bridgmanite compositions with mixed valence states, Fe ²⁺ –Fe ³⁺
88	electronic charge transfer may also create Fe ^{2.5+} states (Mattson and Rossman 1987, Burns
89	1993). Because the separation distance between A and B sites is smaller than between A and
90	adjacent A sites, the activation energy related to the distance of electron migration was suggested
91	to be lower for A-B Fe ²⁺ –Fe ³⁺ charge transfer (Fei et al. 1994). For the same reason, charge
92	transfer is generally expected to be promoted by pressure and impeded by temperature (Mattson
93	and Rossman 1987; Fei et al. 1994; Xu and McCammon 2002; Lobanov et al. 2017). In total, Fe
94	in bridgmanite in Earth's mantle may be distributed among a multitude of different combinations
95	of valence state (Fe ²⁺ , Fe ^{2.5+} , Fe ³⁺), crystallographic site (A1, A2, or B), and spin state (high or
96	low).
97	Controversy over the electronic states of iron in bridgmanite has also been drawn out by different
98	interpretations of a key observational technique, Mössbauer spectroscopy. The Mössbauer effect
99	allows each valence state, coordination environment, and spin state to be distinguished by
100	characteristic values for center shift (CS) and quadrupole splitting (QS) (Dyar et al. 2006).
101	Interpretation of CS and QS obtained at high pressures requires deconvolving poorly-constrained
102	effects of structural and electronic changes. Pressure generally distorts crystallographic sites of
103	bridgmanite, leading to higher QS with pressure (e.g. Lin et al. 2013; McCammon et al. 2013).

Although the existence of the spin transition in Fe ³⁺ in the bridgmanite B-site is now well-
accepted (Lin et al. 2013; Badro 2014), the published values for Mössbauer parameters of low-
spin Fe^{3+} in bridgmanite range from $CS\sim1$ mm/s and $QS\sim3$ mm/s similar to high-spin Fe^{2+}
(Catalli et al. 2010; Gu et al. 2012) to CS<0.5 mm/s and QS \sim 1-1.5 mm/s similar to high-spin
Fe ³⁺ (Jackson et al. 2005; Kupenko et al. 2015; Liu et al. 2018). Predictions by DFT support
higher QS values 2-3 mm/s due to asymmetrical electronic field gradient generated by spin-down
electrons in the B-site, but have not addressed CS of low-spin Fe ³⁺ (Hsu et al. 2011). Depending
on which of these interpretations is correct, low-spin Fe ³⁺ may be misidentified as high-spin Fe ²⁺
or high-spin Fe ³⁺ , or vice versa. The conditions at which the spin transition is reported based on
these observations range from 13-24 GPa (Mao et al. 2015) to 50-70 GPa (Catalli et al. 2010,
2011). Other phenomena suggested to impact Mössbauer spectra of bridgmanite and related
compounds at high pressures include charge-transfer, which should result in enhanced electrical
and thermal conductivity in silicates/perovskites with a mixture of Fe ²⁺ and Fe ³⁺ (Fei et al. 1994;
Xu and McCammon 2002; Keppler et al. 2008; Long et al. 2009), and changes in glasses in
recoil-free fraction of Fe^{2+} and Fe^{3+} , causing shifts in the relative contributions of Fe^{2+} and Fe^{3+}
to spectral area (Prescher et al. 2014). In addition, spectra for complex materials such as
bridgmanite suffer from overlapping peaks and non-unique fitting. These issues may be
addressed by complementary techniques such as X-ray emission spectroscopy and X-ray
diffraction to independently constrain spin state and structure (e.g. Catalli et al. 2010) and
systematic analysis of a range of compositions (e.g. McCammon et al. 2013).
Previous attempts to prepare well-characterized bridgmanite rely on samples synthesized in the
multianvil press, which is typically limited to ~25 GPa. At these conditions, bridgmanite is stable

with only up to ~15-20% Fe (Fei et al. 1996; Tange et al. 2009), and typically exhibits a mixture of Fe²⁺ and Fe³⁺ depending on composition and f_{O2} (e.g. Frost and Langenhorst 2002; Frost et al. 2004). At pressures ~75-100 GPa in the diamond anvil cell, a wider range of compositions with up to at least 75-90% FeSiO₃ and lower Fe³⁺/total Fe becomes stable (Tateno et al. 2007; Dorfman et al. 2012, 2013; Ismailova et al. 2016). The goal of this study is to systematically analyze electronic states of iron-rich bridgmanite using Mössbauer spectroscopy of well-characterized end-member samples. These experiments resolve discrepancies in interpretation of high-pressure Mössbauer spectra of bridgmanite by firmly constraining valence states of iron at 1 bar, where Mössbauer parameters CS and QS are unambiguous. Results address the conditions and observable characteristics of possible spin transitions and charge transfer, and will be important to future characterization of bridgmanite relevant to Earth's deep mantle heterogeneities.

Methods

- Four bridgmanite compositions were examined ranging from 12-100% Fe³⁺/total Fe and from 10-50% Fe/total cations. Bridgmanites were synthesized from the following starting materials:
- 50% enstatite, 50% ferrosilite (En50Fs50) pigeonite was synthesized at the Crystal

 Growth Facility at EPFL in a gas-mixing furnace. A stoichiometric mixture of Fe₂O₃

 (enriched to 48.3% ⁵⁷Fe), MgO and SiO₂ was ground in an agate mortar until

 homogenous and cold-sintered in a 3-ton press at room temperature for 1 minute. The

 resulting pellet was placed in an alumina crucible on a bed of unenriched powder mixture

 of the same composition. The sample was first heated in air at 1000°C, then reduced

under an N ₂ /H ₂ mixture bubbled through H ₂ O at 1100°-1200°C for 3 days, then rapidly
quenched to room temperature. Mössbauer analysis of the starting material was consistent
with complete reduction of ferric iron to ferrous iron, with a detection limit of a few
percent. X-ray diffraction and electron microprobe analysis (Table 1) confirmed that the
oxides transformed to monoclinic $P21/c$ pigeonite with composition $(Mg_{0.52}Fe_{0.48}^{2+})SiO_3$
(0% ferric before bridgmanite synthesis).

- 90% enstatite, 10% hematite (En90Hem10) glass starting material was synthesized from intimately mixed Fe₂O₃ (enriched to 96.6% ⁵⁷Fe), MgO and SiO₂ powders by containerless laser-levitation (Weber et al. 1994) under compressed air at IPGP, Paris. Mössbauer spectroscopy indicates total ferric iron content of the glass before bridgmanite synthesis is ~30%. The homogeneity and composition of the glass were determined by electron microprobe analysis (Table 1), yielding formula for this sample as follows:
 Mg_{0.97}Fe²⁺_{0.14}Fe³⁺_{0.06}Si_{0.90}O₃. Oxygen deficiency in measured formula may be due to use of Fe²⁺-rich standards and few-% uncertainty indicated by 97-98% oxide totals during microprobe measurements.
- 50% enstatite, 50% hematite (En50Hem50) akimotoite synthesis and characterization
 were described in (Liu et al. 2018). Based on microprobe analysis and Mössbauer
 spectroscopy, the formula obtained for this sample is Mg_{0.46}Fe³⁺_{1.04}Si_{0.49}O₃ (100% ferric).
- 75% ferrosilite, 25% corundum (Fs75Co25, or almandine-composition) glass synthesis and characterization were described in Dorfman et al. (2016). The composition of the glass, normalized to 3 oxygens, is Fe²⁺_{0.55}Fe³⁺_{0.12}Al_{0.54}Si_{0.73}O₃ (20% ferric before bridgmanite synthesis).

Starting materials were loaded as crystalline powder or glass chip in diamond anvil cells with
100-150-micrometer culet and 300-micrometer bevel. Each sample was contained in a 30-50-
micrometer hole drilled in a Re gasket. To insulate the samples during laser heating and transmit
quasi-hydrostatic stress, En50Fs50 and Fs75Co25 were loaded sandwiched between platelets of
NaCl; En90Hem10 was loaded in Ar gas at the EPFL; and En50Hem50 was loaded in Ne gas
using the COMPRES/GSECARS gas loading system (Rivers et al. 2008). Pressure during
experiments up to ~100 GPa was measured by Raman spectroscopy of the stressed diamond
anvil culet center (Akahama and Kawamura 2006), or for En50Hem50 a ruby sphere loaded with
the sample (Mao et al. 1986).
Bridgmanite was synthesized from Fs75Co25, En50Fs50, and En90Hem10 compositions as in
previous studies (Dorfman et al. 2012, 2013) by laser heating to 2000-2500 K for ~20-60 min
after compression at 300 K directly to ~75-100 GPa. The transformation and homogeneity of
each sample was confirmed by X-ray diffraction at beamlines ID27 and ID09 (λ =0.3738 Å and
0.4117 Å or 0.4155 Å, respectively) of the ESRF (Figure 1). Minor CaCl ₂ -type SiO ₂ diffraction
peaks are also observed in some samples after laser heating. As described by Liu et al. (2018),
the En50Hem50 akimotoite starting material transforms reproducibly and reversibly to
bridgmanite at 300 K and 22-26 GPa, so this sample was simply compressed at 300 K.
Energy-domain Mössbauer spectroscopy was performed at the Nuclear Resonance beamline
ID18 of the European Synchrotron Radiation Facility (Rüffer and Chumakov 1996; Potapkin et
al. 2012) and the COMPRES/sector 3 offline Mössbauer spectroscopy laboratory at the
Advanced Photon Source at Argonne National Laboratory. At ID18, incident light is synchrotron
X-rays monochromatized by a ⁵⁷ FeBO ₃ single crystal to the ⁵⁷ Fe resonant energy of 14.4 keV

with energy resolution of \sim 5.5 neV. The X-ray beam is focused to \sim 9x14 micrometers full width at half maximum. At the sector 3 offline Mössbauer laboratory, incident gamma-rays are provided by a 400-micrometer-diameter radioactive 57 Co point source. To generate a range of energies for absorption spectroscopy measurements, both the 57 FeBO₃ monochromator at ID18 and the 57 Co at sector 3 are oscillated +/- 5mm/s (1 bar measurement at sector 3 used +/- 10 mm/s). Source velocities are calibrated with an α -Fe foil standard at 300 K. Synchrotron source line width and center shift are calibrated with a K_2Mg^{57} Fe(CN) $_6$ standard before and after each measurement. The linewidth for the conventional measurements was set to match a 6-month-old radioactive point source. Synchrotron Mössbauer spectra were collected for \sim 2-8 hrs at each pressure. Conventional Mössbauer spectra were obtained for \sim 2 weeks each. Spectra were fit to pseudo Voigt doublets using MossA software (Prescher et al. 2012). All spectra were fit using a full transmission integral to account for thicknesses of radiation sources and samples.

Results and discussion

To ensure no change in valence states of Fe across the measured pressure range, all Mössbauer spectroscopy measurements were performed at 300 K and no additional heating was applied to samples after synthesis of bridgmanite. Upon laser heating, both structural transformation and redox may occur. Although some previous studies assume Fe³⁺/total Fe does not change during synthesis (e.g. Nishio-Hamane et al. 2007; Lundin et al. 2008; Dorfman et al. 2013), redox during laser heating is confirmed by our data to result in differences in Fe³⁺/total Fe in synthesized bridgmanite relative to starting materials. During 300 K compression and decompression, we assume that kinetics do not permit site-site diffusion and redox reactions. Therefore, Fe³⁺/total Fe for bridgmanites synthesized at high pressure may be fixed to values 10

213

214

215

216

217

218

219

220

221

222

223

224

225

226

227

228

229

230

231

232

233

234

observed after 300 K decompression to 1 bar (these Fe³⁺/total Fe values are reported here in figures and tables). Mössbauer spectra were measured for Fs75Co25, En50Fs50, and En90Hem10 bridgmanites on decompression from ~75-100 GPa in ~25 GPa steps to 1 bar (Figures 2-4 a-c). En50Hem50 akimotoite was observed upon compression from 1 bar to bridgmanite at 32 and 70 GPa (Figures 2-4 d). Changes in the Mössbauer parameters of each bridgmanite composition during 300 K compression/decompression (Table 2, Figure 5) may be due to 1) electronic spin transitions, 2) pressure-induced structural changes including site distortion or amorphization, or 3) charge transfer between nearby Fe ions. The spin transition in Fe³⁺ Effects of the high-to-low spin transition on Mössbauer parameters of Fe³⁺ in bridgmanite may be clearly observed in En50Hem50 bridgmanite, for which the spin transition in the octahedral site has been documented at ~48 GPa at 300 K by X-ray diffraction and X-ray emission spectroscopy (Liu et al. 2018). En50Hem50 bridgmanite is 100% Fe³⁺, with 50% Fe in the pseudo-dodecahedral site, and 50% Fe in the octahedral site. Mössbauer spectra at high pressure exhibit two closely-overlapping doublets, with absorption at \sim -0.4-0.0 mm/s and \sim 0.6-1 mm/s (Figure 3d, Figure 4d). Across the pressure-induced spin transition from 32 to 70 GPa, spectra change slightly: average CS decreases by 0.15 mm/s and QS increases by 0.35 mm/s. Two reasonable fits to these data are possible for a sample with pure Fe³⁺: either Fe³⁺ in A- and Bsites adopt CS differing by <0.05 mm/s with contrasting QS, 0.6-0.9 and 1.4-1.8 mm/s, or the difference in CS is larger, ~0.4 mm/s, while QS is identical within ~0.5 mm/s. Neither option is

consistent with a large change across the spin transition to QS ~3 mm/s predicted in bridgmanite

by DFT (Hsu et al. 2011). At 32 GPa (Figure 3d), the fit with contrasting CS would produce

CS=0.45 mm/s for the higher CS component, which would be high for Fe ³⁺ (Figure 5). We
therefore favor a fit with contrasting QS for high-spin Fe ³⁺ in A-site vs. B-site, consistent with
the different asymmetry of the two sites in high-spin state. At 70 GPa (Figure 4d), the overall
decrease in CS allows a fit with contrasting CS with acceptable Mössbauer parameters for Fe ³⁺
for both sites, where the low-spin B-site Fe ³⁺ exhibits lower CS and higher QS relative to high-
spin B-site Fe ³⁺ at lower pressure. In addition, recent data for well-characterized samples indicate
that pressure tends to increase QS (i.e. level of structural distortion around the iron ion
increases), and the principal change in Mössbauer parameters of octahedrally-coordinated Fe ³⁺
across the spin transition is a decrease in CS (i.e. density of electrons around the iron nucleus
increases) (Pasternak et al. 2002; Kupenko et al. 2015; Liu et al. 2018) (Table 3). We thus obtain
$CS \sim 0.35$ mm/s for high-spin Fe^{3+} in both sites at 32 GPa below the spin transition, and a lower
CS -0.07 mm/s for low-spin Fe ³⁺ at 70 GPa (Table 2, Figure 5).
These results can be used to determine whether spin transitions occur in other compositions with
mixed valence states of iron. For less Fe ³⁺ -rich En50Fs50 and En90Hem10 compositions, Fe ³⁺
doublets can be interpreted based on values observed at similar conditions for En50Hem50. The
64
fit uncertainty for Fe ³⁺ doublets in En50Fs50 at 75 GPa is large (as much as ~1 mm/s) due to
overlap with other doublets, but the refined value 0.4 mm/s is consistent with high-spin Fe ³⁺ in
overlap with other doublets, but the refined value 0.4 mm/s is consistent with high-spin Fe ³⁺ in
overlap with other doublets, but the refined value 0.4 mm/s is consistent with high-spin Fe^{3+} in the A-site, as expected with a (Mg+Fe)/Si ratio \sim 1 and B-site filled with Si. For En90Hem10,
overlap with other doublets, but the refined value 0.4 mm/s is consistent with high-spin Fe^{3+} in the A-site, as expected with a (Mg+Fe)/Si ratio ~1 and B-site filled with Si. For En90Hem10, with ~50% Fe^{3+} , stronger, better-resolved Fe^{3+} exhibits a slight decrease in CS, from 0.34 mm/s

transition is consistent with the more Si-depleted composition with space available for Fe³⁺ in the
 B-site.

Site distortion

All Fe²⁺-bearing bridgmanite compositions exhibit splitting at lower-mantle pressures consistent with predictions of distortion of the A-site (Hsu et al. 2010). At pressures above 1 bar for Fe²⁺-rich Fs75Co25 and En50Fs50 compositions, absorption at ~2-3 mm/s requires two Fe²⁺ sites (Figure 3a,b, Figure 4a,b). QS of both sites increases with pressure (Figure 5) and the relative weight of the higher-QS site increases, in accord with increasingly asymmetric A-sites. At ~75 GPa in these compositions, ~1/3 of the Fe²⁺ sites exhibit QS=3.8-3.9 mm/s, with the remaining Fe²⁺ at QS=2.1-2.5 mm/s. For Fe³⁺ in the A-site, QS remains relatively constant with pressure. However, spectral resolution does not allow us to either confirm or disprove development of multiple Fe³⁺ A-sites due to site distortion (Hummer and Fei 2012).

269 Charge transfer (Fe^{2.5+})

The signature of charge transfer, i.e. increased delocalization of electrons between iron ions, is observed in Fe compositions Fs75Co25 and En50Fs50 as an absorption peak at \sim 1.6 mm/s (Figure 2a, Figure 3a, Figure 4a-b). This peak can be fitted with a doublet with CS \sim 0.8 and QS \sim 1.6, intermediate between typical parameters observed for Fe²⁺ and Fe³⁺ and similar to Fe^{2.5+} as previously identified in bridgmanite (Fei et al. 1994; Xu and McCammon 2002) (Figure 7). The Fe^{2.5+} doublet intensity is interpreted to represent 50% Fe²⁺ and 50% Fe³⁺ when calculating Fe³⁺/total Fe (Figure 6b). This assumption yields constant Fe³⁺/total Fe with 300 K compression/decompression for all compositions within \sim 10% error entailed in fitting site weights, indicating no change in total redox state with pressure.

In general, the favorability of charge transfer would be expected to depend on whether Fe ²⁺ and
Fe ³⁺ occupy neighboring sites (note that Fe-rich En50Hem50 does not exhibit charge transfer
because all Fe is Fe ³⁺) and how much energy is required for electrons to hop between these sites.
As noted in previous work (Fei et al. 1994), the shortest site-site distances for electron migration
in the bridgmanite structure are between face-sharing B-sites and A-sites. However, the iron-rich
compositions examined in this study incorporate at least enough Al and Si to fill the B-site, and
are expected to accommodate both Fe^{2+} and Fe^{3+} in the A-site. The face-sharing A-A site
distance in Fe-rich bridgmanite, based on lattice parameters determined by X-ray diffraction
(Dorfman et al. 2012, 2013), is \sim 10% larger than the face-sharing A-B site distance, but
comparable to edge-sharing octahedra in chain silicates at 1 bar known to exhibit Fe^{2^+} - Fe^{3^+}
charge transfer (Mattson and Rossman 1987).
In the Fs75Co25 composition, Fe ^{2.5+} completely replaces Fe ³⁺ at all pressures at 300 K. Even at 1
bar, \sim 20% of the spectral weight is a component with CS=0.6 mm/s, too high for Fe ³⁺ and
consistent with $Fe^{2.5+}$ (Figure 7). With increasing pressure, the intensity of the $Fe^{2.5+}$ component
is constant within uncertainty, though the Mössbauer parameters are more uncertain due to
overlap. Rietveld refinement of atomic positions (Dorfman et al. 2012) confirms that all Fe in
this composition resides in the A-site. As a result, charge transfer in this composition must take
place between face-sharing A-site Fe ²⁺ and A-site Fe ³⁺ .
For En50Fs50-composition bridgmanite, Fe ²⁺ -Fe ³⁺ neighboring A-sites will be diluted by Mg in
the A-site, and charge transfer appears to be possible but less favorable. A charge transfer
component accounting for $\sim 1/3$ of the Fe ³⁺ is needed to fit data obtained at ~ 75 GPa (Figure 4b).
Although Fe ²⁺ -Fe ³⁺ neighboring A-sites would be expected to be nearly as common in En50Fs50

301	as in Fs75Co25, a separate Fe ³⁺ doublet is still observed, and upon decompression to pressures
302	25 GPa and below the Fe ^{2.5+} component disappears (Figure 3a,b). Weights of Fe ^{2.5+} and Fe ³⁺ sites
303	at all conditions are consistent with the 1 bar Fe ³⁺ /total Fe (Figure 6b). These observations
304	suggest a pressure-driven crossover in the stability of charge transfer in this composition.
305	Compression of adjoining sites is expected to lower energy required for electron transfer (Fei et
306	al. 1994; Xu and McCammon 2002). The mobility of electrons between A-sites appears to
307	increase accordingly between 25 and 75 GPa. Observations of charge transfer in En50Fs50
308	relative to Fs75Co25 bridgmanite these samples indicate that charge transfer is promoted by
309	pressure and high Fe concentration.
310	Evidence for charge transfer in En90Hem10-composition bridgmanite, which is also mixed-
311	valence but relatively Fe-poor and has (Mg+Fe)/(Al+Si) ratio greater than 1, is not clear (Figure
312	4c). A Fe ²⁺ site with CS~0.8 at high pressures is observed in En90Hem10 composition, but broad
313	peaks, high QS, and no change in intensity of Fe ³⁺ doublets when this doublet appears (Figure
314	6b, Table 2) all suggest the CS 0.8 mm/s doublet is more likely to represent Fe ²⁺ in
315	untransformed glass starting material. In contrast to the Fe ²⁺ -rich compositions Fs75Co25 and
316	En50Fs50, in the En90Hem10 composition the \sim 50% Fe ²⁺ and 50% Fe ³⁺ are expected to occupy
317	the A- and B-sites respectively due to the higher (Mg+Fe)/(Al+Si) ratio, so charge transfer would
318	take place between A- and B-sites rather than two A-sites. Even for this lower Fe concentration,
319	Fe ²⁺ -Fe ³⁺ neighboring sites would be expected to be common: the probability that none of the 8
320	B-sites surrounding Fe^{2+} in the A-site is Fe^{3+} should be ~50%. Under these conditions A-B site
321	charge transfer is not evident, though the presence of an overlapping Fe ^{2.5+} doublet cannot be
322	ruled out. In contrast to intuition based on electron migration distance (Fei et al. 1994), charge

323

324

325

326

327

328

329

330

331

332

333

334

335

336

337

338

339

340

341

342

transfer appears to be more favorable between face-sharing A-sites than between face-sharing A- and B-sites. Although the distance between A-sites is longer, the enthalpy cost of moving an electron into the highly-compressed B-site (effectively, Fe²⁺ in B and Fe³⁺ in A) may provide an explanation for a failure to observe A-B charge transfer.

Implications

If previous studies of physical properties of bridgmanite have misidentified or missed spin transitions based on incorrect assignment of sites observed by Mössbauer spectroscopy. predicted seismic velocities for iron-bearing lower mantle phase assemblages may be systematically offset. The greatest effects of valence states of iron on geophysical properties are likely to be observed in the shallow lower mantle due to softening during the spin transition for Fe³⁺-bearing compositions (Shukla et al. 2016) and higher contrast in bulk compressibility and density between Fe²⁺- and Fe³⁺-rich bridgmanite at pressures at and below the Fe³⁺ spin transition (Liu et al. 2018). At greater depths above the spin transition pressure range, seismic velocities of Fe²⁺- and Fe³⁺-rich bridgmanite converge. While speciation of Fe will also affect partitioning of Fe between bridgmanite and ferropericlase in the mantle (e.g. Piet et al. 2016), the net effect of multiple orders of magnitude difference in bridgmanite-ferropericlase partition coefficient on density contrast is only 0.1% (Ricolleau et al. 2009; Dorfman and Duffy 2014). suggesting that effects of partitioning on elastic properties are too subtle to be observed via seismology. Attempts to use seismology to map the redox conditions of the lower mantle should focus on depths below the spin transition pressure, between 660 and 1000 km.

The dependence of charge transfer in mantle bridgmanite on composition and pressure may not
significantly affect elastic properties, but could result in regional- and depth-variation of
transport properties including electrical and thermal conductivity. A-A site charge transfer
should have no effect on density of the bridgmanite structure as the overall site occupancy
remains the same. A-B site charge transfer would decrease density by expanding the B-site, but
based on our data, we infer that this mechanism is not significant in Earth's mantle. Either
mechanism of charge transfer, along with other mechanisms including conductivity of vacancies
and ions, will contribute to electrical and thermal conductivity (Xu and McCammon 2002). Our
observations do support enhancement of charge transfer by Fe-enrichment and high pressures
corresponding to the deep lower mantle—both likely characteristics of dense heterogeneities
(Ishii and Tromp 1999; Lau et al. 2017) and basalt-rich slabs near the core-mantle boundary
(e.g.Grand 2002). In addition, the very deep lower mantle has been suggested to host mixed-
valence bridgmanite, even under reduced conditions in contact with metallic iron from the outer
core (Shim et al. 2017). Regions rich in subducted basalt will have higher Al- and Si-content,
which is more likely to stabilize mixed-valence iron in the bridgmanite A-site. Basalt graveyards
could thus more efficiently conduct heat from the outer core, with corresponding effects on the
formation of thermochemical plumes and entrainment of subducted material. As the densest
heterogeneities identified in the lower mantle, ULVZs resting on the core-mantle boundary are
likely Fe-rich (e.g. Rost et al. 2005; Brown et al. 2015), but their redox states are not well-
constrained by available geophysical data. Proposed compositions for ULVZs include
enrichment in metallic melt (Williams and Garnero 1996; Liu et al. 2016) or iron-rich oxide
(Wicks et al. 2010; Hu et al. 2016; Liu et al. 2017) or silicate (Mao et al. 2006). However, the

high temperatures expected at the base of the mantle may impede charge transfer (Mattson and Rossman 1987, Xu and McCammon 2002), and additional mechanisms such as conductivity of vacancies and ions will be increasingly important at high temperatures (Xu and McCammon 2002). Future experimental studies will also need to quantify charge transfer in lower-mantle post-perovskite. If observed, enhanced electrical and thermal conductivity of ULVZs may indicate either the presence of Fe metal or charge transfer due to mixed-valence Fe-rich bridgmanite. Distinguishing these hypotheses is important to constraining redox evolution at the core-mantle boundary.

Acknowledgements

The authors thank Susanne Seitz for assistance with microprobe analysis of starting materials at the University of Lausanne. We thank Richard Gaal for assistance with gas loading at the EPFL and Sergey Tkachev for assistance at the APS. Use of the COMPRES-GSECARS gas loading system and the APS offline Mössbauer laboratory facilities was supported by COMPRES under NSF Cooperative Agreement EAR-1606856 and by GSECARS through NSF grant EAR-1634415 and DOE grant DE-FG02-94ER14466. ⁵⁷Co-source Mössbauer spectroscopy was performed at the APS beamline 3-ID Mössbauer Laboratory. This research used resources of the Advanced Photon Source, a U.S. Department of Energy (DOE) Office of Science User Facility operated for the DOE Office of Science by Argonne National Laboratory under Contract No. DE-AC02-06CH11357. We thank the European Synchrotron Radiation Facility (Grenoble, France) for provision of synchrotron radiation at beamlines ID18 for synchrotron Mössbauer spectroscopy, and beamlines ID09 and ID27 for synchrotron X-ray diffraction. Laser heating was performed at beamline ID24 of the ESRF with assistance from Innokenty Kantor. S. M. Dorfman 18

acknowledges funding support from the Marie Heim-Vögtlin program of the Swiss National Science Foundation through project PMPDP2_151256 and the National Science Foundation project EAR-1664332.

Figure and table captions

Figure 1: X-ray diffraction patterns for bridgmanites obtained after laser heating and before decompression with energy-domain SMS, with diffraction angle converted to lattice spacing (d) to account for differences in diffraction wavelength. Diffraction peaks from medium (N=NaCl, and Ar for En90Hem10 sample) and minor stishovite (St) are identified, and black sticks below comprise bridgmanite reference pattern.

Figure 2: Observed Mössbauer spectra at 1 bar. For compositions in a) b) and c), synchrotron Mössbauer spectra are obtained at ESRF ID18 from iron-bearing bridgmanite samples recovered to 1 bar after 300 K decompression from high-pressure synthesis. In d), conventional ⁵⁷Co Mössbauer spectrum is obtained at APS sector 3 offline lab from synthetic akimotoite before 300 K compression. Blue doublets=Fe²⁺. Red doublets=high spin Fe³⁺. Purple doublets=Fe^{2.5+} charge transfer component. Original data are black points, with total fit indicated by red curve and misfit by red points.

Figure 3: Observed Mössbauer spectra for iron-bearing bridgmanite at high pressure \sim 27 GPa below the spin transition in Fe³⁺. Spectra shown in a) b) and c) use synchrotron Mössbauer source at ESRF ID18 (total Fe³⁺/total Fe listed for each composition is assumed to be same as 1 bar recovered sample), while d) uses conventional ⁵⁷Co Mössbauer source at APS sector 3 offline lab. Blue doublets=Fe²⁺ (where darker blue indicates distorted A-site with high QS, and

408	lighter blue Fe ²⁺ in untransformed glass in En90Hem10 composition in c)). Red doublets=high
409	spin Fe ³⁺ . Purple doublets=Fe ^{2.5+} charge transfer component. Original data are black points, with
410	total fit indicated by red curve and misfit by red points.
411	Figure 4: Observed Mössbauer spectra for iron-bearing bridgmanite at high pressure ~72 GPa
412	above the spin transition in Fe ³⁺ . Spectra shown in a) b) and c) use synchrotron Mössbauer
413	source at ESRF ID18 (total Fe^{3+} /total Fe listed for each composition is assumed to be same as 1
414	bar recovered sample), while d) uses conventional ⁵⁷ Co Mössbauer source at APS sector 3
415	offline lab. Blue doublets=Fe ²⁺ (where darker blue indicates distorted A-site with high QS, and
416	lighter blue Fe ²⁺ in untransformed glass in En90Hem10 composition in c)). Red doublets=high
417	spin Fe ³⁺ , and pink=low spin Fe ³⁺ . Purple doublets=Fe ^{2.5+} charge transfer component. Original
418	data are black points, with total fit indicated by red curve and misfit by red points.
419	Figure 5: Mössbauer parameters a) quadrupole splitting (QS) and b) center shift (CS) observed
420	for bridgmanite as a function of pressure for all sites in all compositions. Symbols indicate bulk
421	composition of each bridgmanite sample (diamonds: Fs75Co25, squares: En50Fs50, circles:
422	En90Hem10, triangles: En50Hem10), while colors indicate spin and valence state of iron (blue:
423	Fe ²⁺ , purple: Fe ^{2.5+} (charge transfer), red: high-spin Fe ³⁺ , light pink: low-spin Fe ³⁺ , magenta:
424	mixed-spin Fe ³⁺ (overlap between doublets impedes resolution of separate high- and low-spin
425	doublets).
426	Figure 6: a) Relative total amount of high-spin iron in each sample as a function of pressure,
427	based on sum of area of all high-spin Fe ²⁺ , Fe ^{2.5+} , and Fe ³⁺ doublets. b) Relative total amount of
428	Fe ³⁺ in each sample as a function of pressure, based on area of Fe ³⁺ doublets plus half the area or

429	charge transfer component. Error bars represent 2σ obtained from fit of Mössbauer spectral
430	intensity.
431	Figure 7: Mössbauer parameters observed for Fe in bridgmanite and other compounds. Results
432	from this study for Fe ²⁺ =blue circles, high-spin Fe ³⁺ =red up-pointing triangles, low-spin
433	Fe ³⁺ =pink down-pointing triangles, charge transfer (Fe ^{2.5+}) component=purple diamonds. Error
434	bars represent fit uncertainty for each doublet. Predicted values for QS from density functional
435	theory for Fe ²⁺ from (Hsu et al. 2010) and for Fe ³⁺ from (Hsu et al. 2011). Shaded regions
436	comprise envelope of observations from previous studies: (Greenwood and Gibb 1971; Pasternak
437	et al. 2002; Hummer and Fei 2012; McCammon et al. 2013).
438	Table 1: Microprobe composition analysis of starting materials performed at the University of
439	Lausanne. Standards used to quantify SiO ₂ , MgO, and FeO were forsterite, fayalite and
440	orthopyroxene. Oxide totals for glass were consistently less than 100%, potentially due to use of
441	Fe ²⁺ -rich standards, higher Fe ³⁺ -content in glass, and matrix effects. Measurements with totals
442	less than 97% were dropped. FeO vs. FeO _{1.5} was determined by Mössbauer spectroscopy at
443	ambient conditions.
444	Table 2: Mössbauer parameters observed for bridgmanite. CS and QS in units of mm/s. *
445	indicates parameters constrained to equal values to aid fit convergence. Note that Fe ^{2.5+} fraction
446	can be assumed to represent 50% $Fe^{2+} + 50\% Fe^{3+}$.
447	Table 3: Hyperfine parameters of high- and low-spin Fe ³⁺ in perovskites obtained by energy-
448	domain Mössbauer spectroscopy.

Tables and figures

450 Table 1

	En50Fs50 (p	igeonite)	En90Hem10 (glass)		
	Weight % oxides	Cations normalized to 3 O (3% Fe ³⁺)	Weight % oxides	Cations normalized to 3 O (30% Fe ³⁺)	
SiO ₂	52.0(2)	0.996	49.2(2)	0.900	
MgO	18.1(2)	0.519	35.4(4)	0.965	
FeO	30.3(2)	0.478	13.31(18)	0.143	
FeO _{1.5}		0.015		0.061	
Total	100.4(4)	1.993	97.8(6)	2.069	

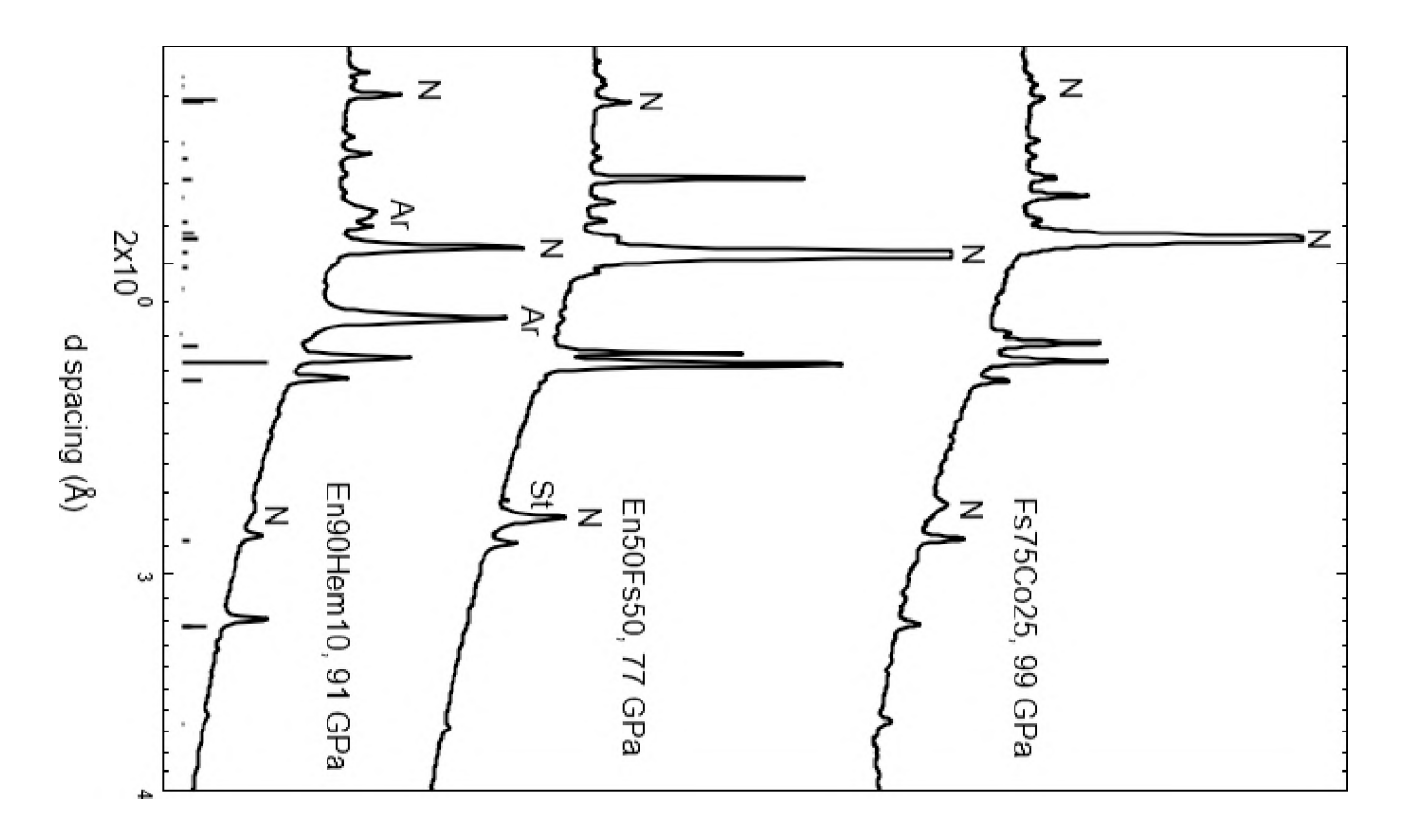
452 Table 2

	Fs75Co25			En50Fs50				
	1 bar			1 bar				
	Fe ²⁺		Fe ^{2.5+}	Fe ²⁺		Fe ³⁺ HS		
CS			0.60(8)	1.06(3)		0.39(3)		
(mm/s)	. ,							
QS	2.01(7)		1.06(20)	1.96(6)		0		
(mm/s)								
Weight	80(11)		20(11)	72(6)		28(6)		
	15 GPa			25 GPa				
	Fe ²⁺		Fe ^{2.5+}	Fe ²⁺		Fe ³⁺ HS		
CS	1.089*	1.089*	0.84(15)	1.21(5)	1.08(3)	0.2(3)		
	(18)	(18)						
QS	3.66(8)	2.34(2)	1.2(3)	2.69(11)	1.73(9)	1.0(4)		
Weight	6(9)	76(17)	17(16)	52(27)	26(21)	22(21)		
	76 GPa		T	75 GPa				
	$\mathrm{Fe^{2^+}}$		Fe ^{2.5+}	Fe ²⁺	_	Fe ^{2.5+}	Fe ³⁺ HS	
CS	0.998(9)	1.0(3)	0.6(2)	0.985(8)	1.00(4)	0.9(9)	0.4 (10)	
QS	3.926	2.4(4)	1.7(7)	3.90(2)	3.1(3)	1.6	0.7 (19)	
	(19)					(1.9)		
Weight	28(14)	54(20)	18(19)	20(27)	43(28)	18(17)	18(18)	
				T				
	En90Hem	10		-	En50Hem50			
	1 bar				1 bar			
	Fe ²⁺		Fe ³⁺ HS		Fe ³⁺ HS			
CS	1.02(7)		0.42(9)	$\overline{}$	0.36(3)			
QS	1.96(19)		0.95(16)		0.73(5)			
Weight	47(9)		53(9)		100			
	36 GPa				32 GPa Fe ³⁺ A HS Fe ³⁺ B HS			
	Fe ²⁺		Fe ³⁺ HS				[S	
CS	1.2(8)	0.8(7)	0.34(3)		0.35(2)		0.32(3)	
QS	QS 3.1(1.7) 2.3(1.4)		1.02(6)	1.37(11)	1.37(11)		0.59(10)	
Weight	22(14)	25(18)	52(16)	0.5*		0.5*		
	67 GPa			70 GPa				
	Fe ²⁺		Fe ³⁺ mixed	Fe ³⁺ A HS		Fe ³⁺ B LS		
CS	1.0(3) 0.81(13)		0.29(3)	0.38(9)		-0.07(10)		
QS	3.3(3) 2.3(7)		1.13(9)	1.35(4)		1.30(5)		
Weight	Weight 20(17) 31(16)		50(15)	0.5*		0.5*		

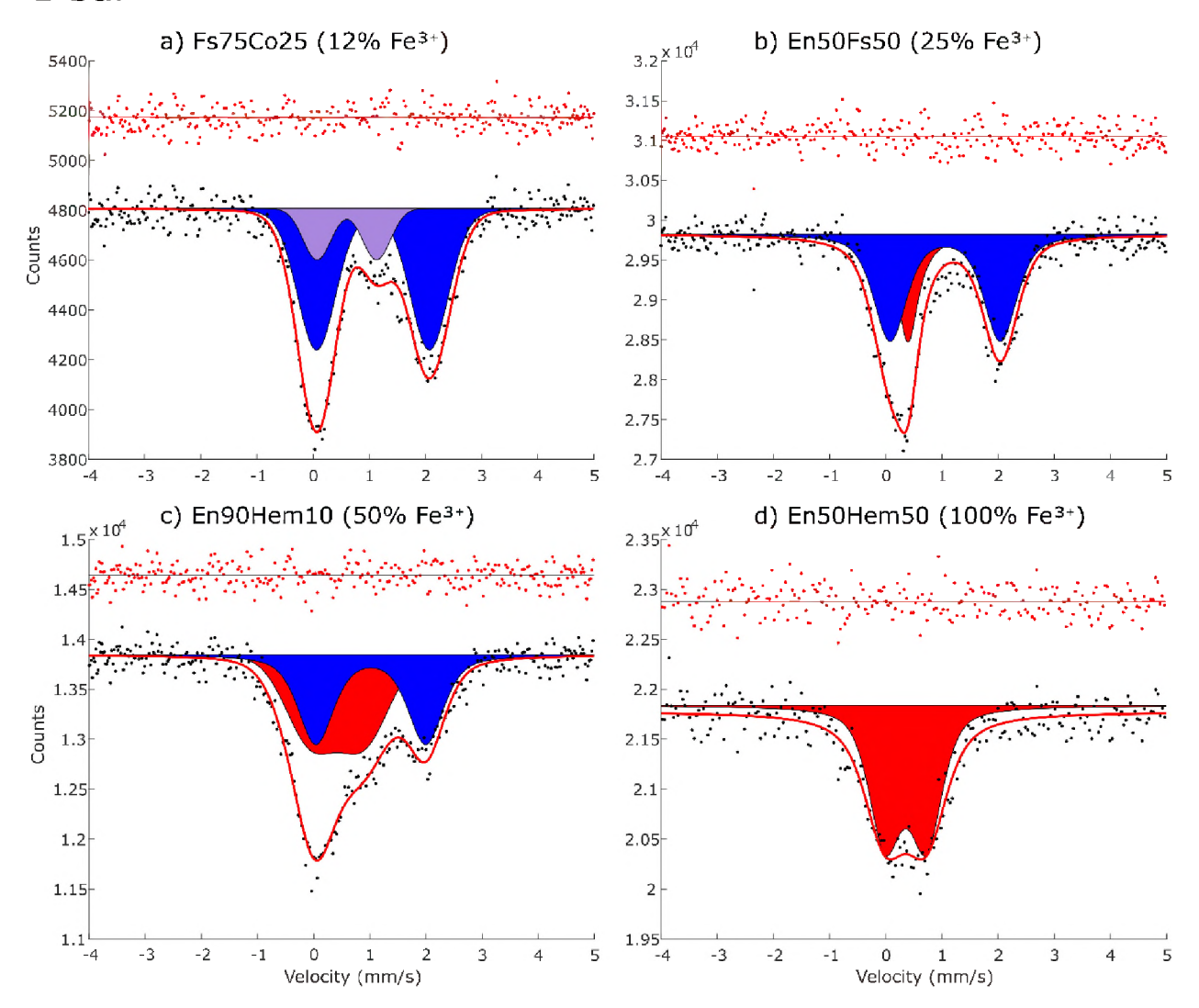
455 Table 3

	HS CS (mm/s)	HS QS (mm/s)	LS CS (mm/s)	LS QS (mm/s)	Reference
Bridgmanite (Mg,Fe,Al) (Fe,Al,Si)O ₃	0.0-0.5	0.3-1.7	N/A	N/A	(Hummer and Fei 2012)
	0.4	1.2-1.5	N/A	N/A	(Potapkin et al. 2013)
	0.4	0.8-1.3	-0.1	0.9	(Kupenko et al. 2015)
	0.1-0.15 (ΔIS A-B)	1.1-1.2	0.3 (ΔIS A-B)	1.3-1.4	(Liu et al. 2018)
	0.2-0.4	0.6-1.4	0.0	1.3	This work
Perovskite- structured rare-earth orthoferrites	0.22-0.24	0.24-0.59	0.04-0.23	0.55-1.42	(Pasternak et al. 2002)

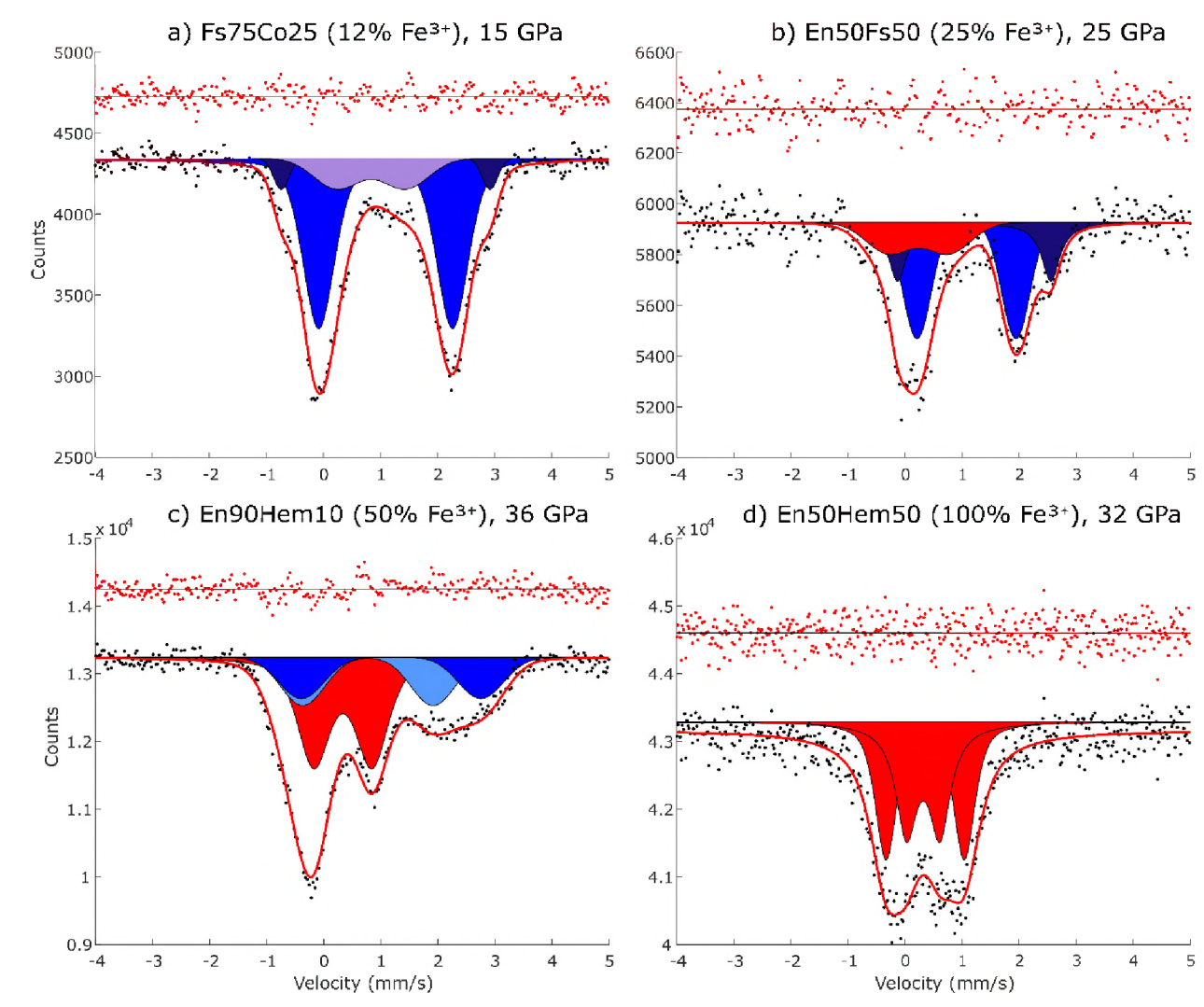
Intensity (arbitrary units)



1 bar



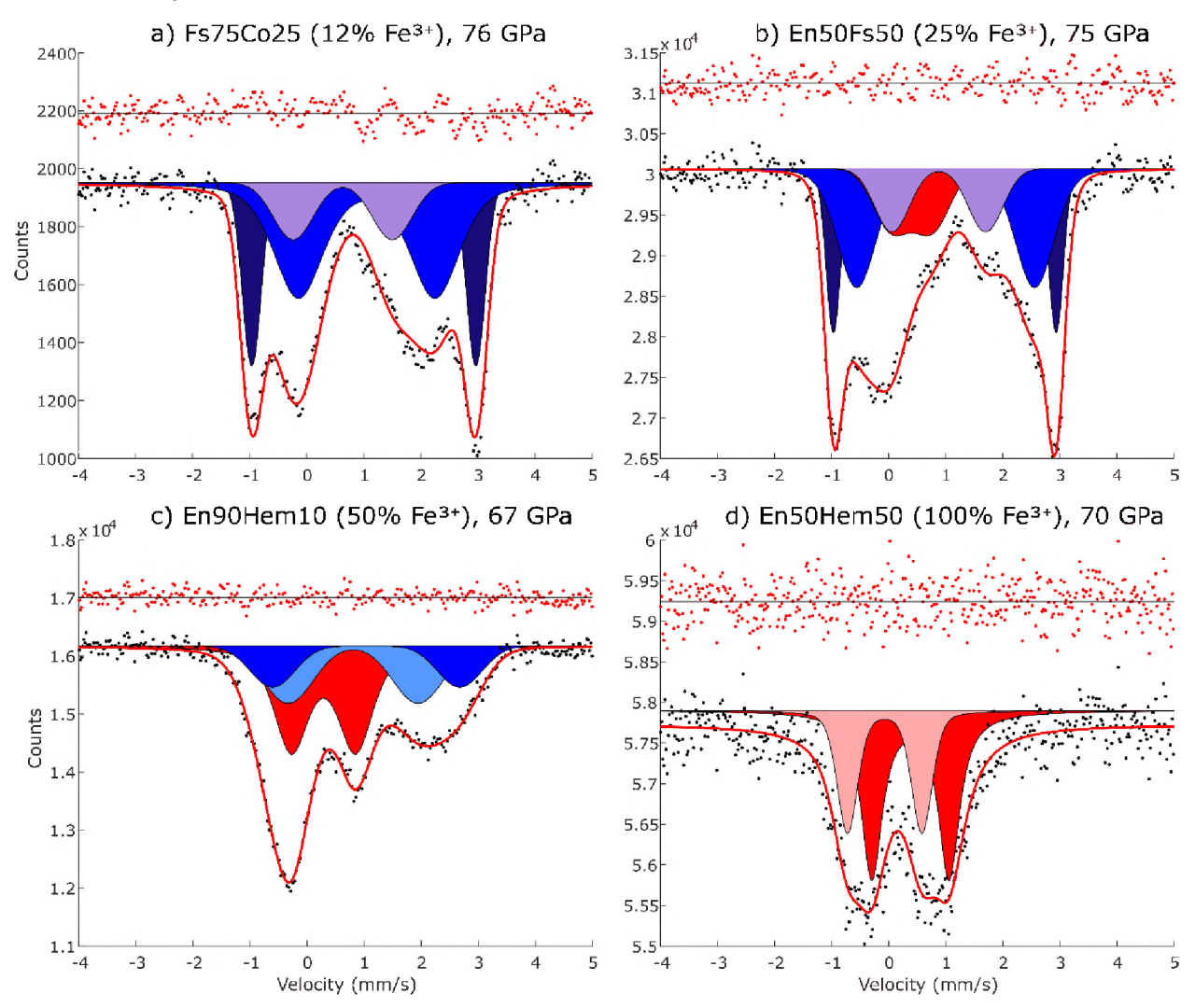
Below spin transition

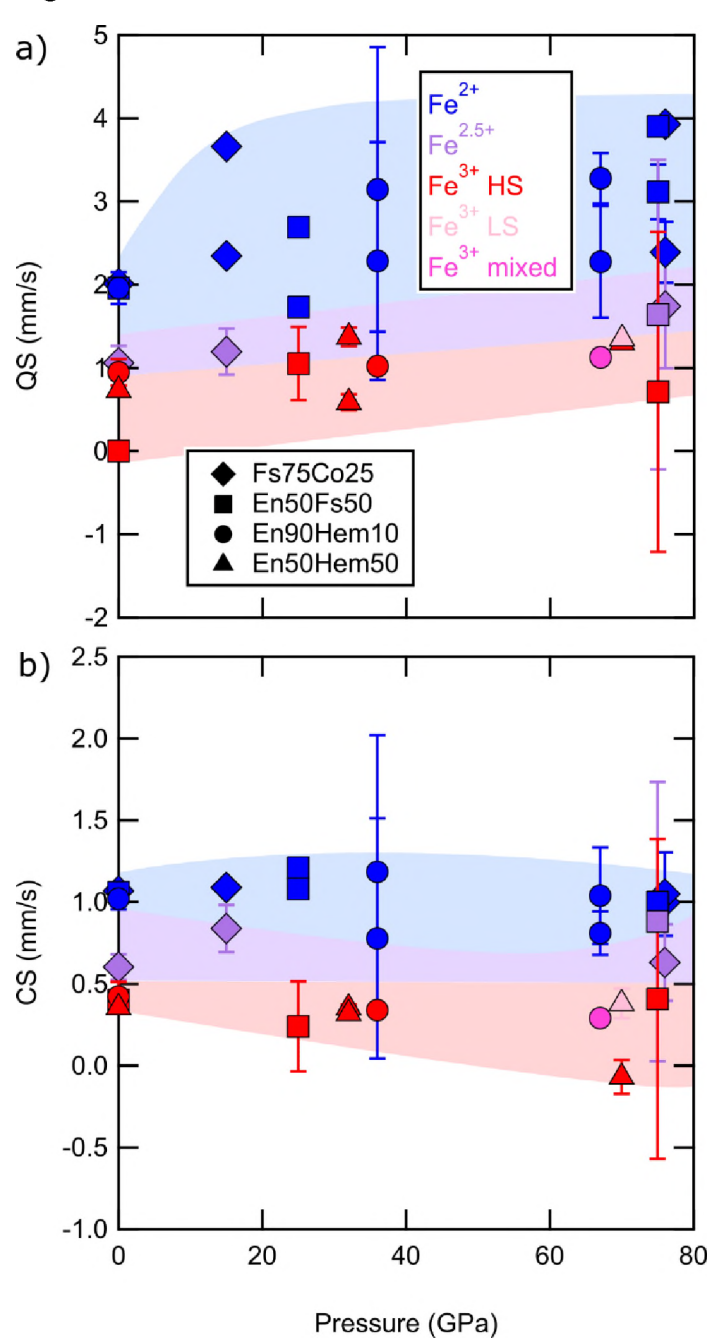


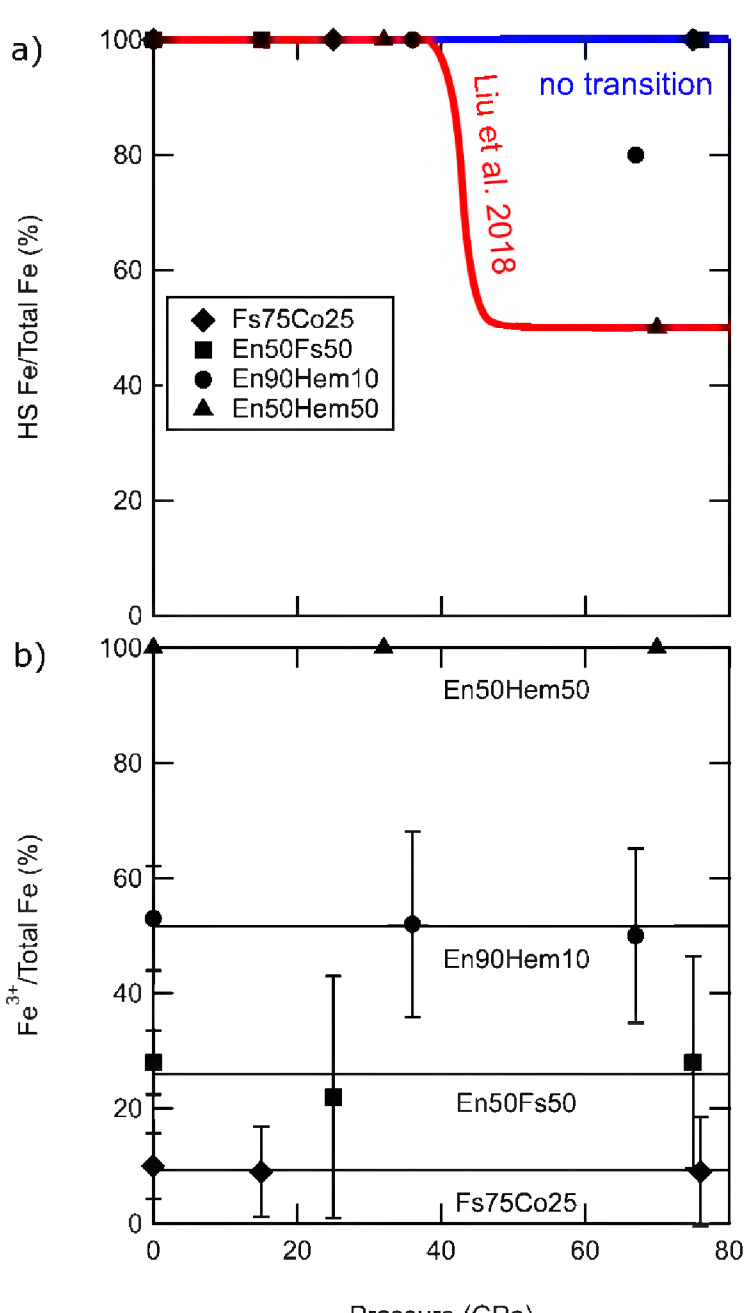
27

463

Above spin transition

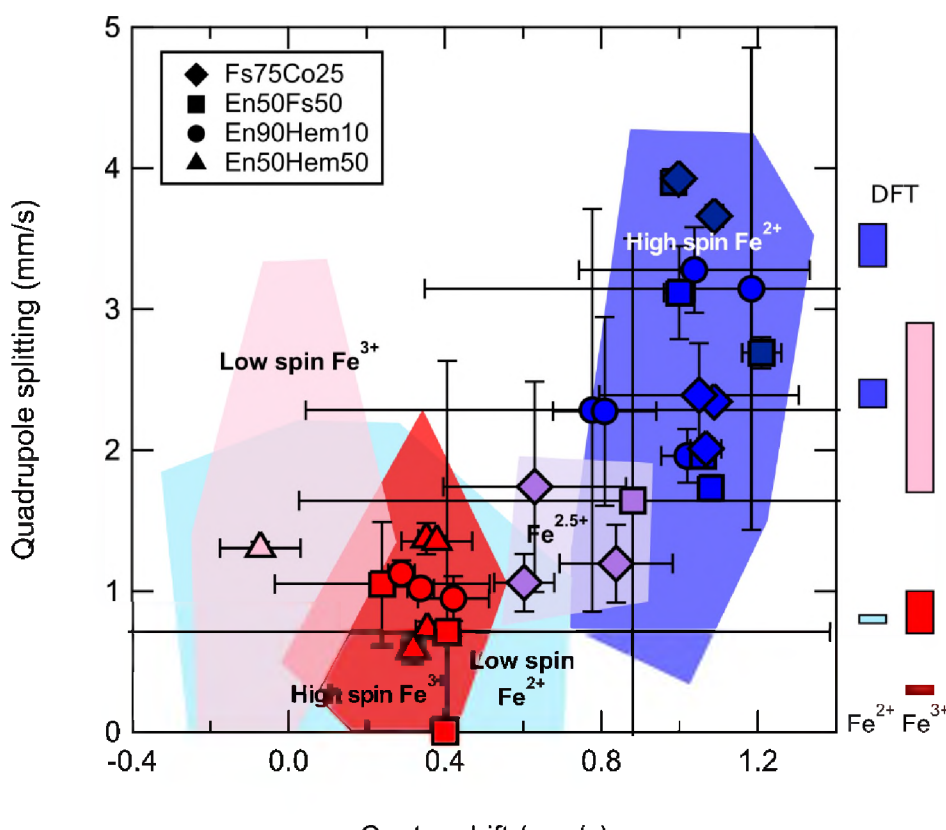






473 Pressure (GPa)

475



477 Center shift (mm/s)

479	References
480 481	Akahama, Y., and Kawamura, H. (2006) Pressure calibration of diamond anvil Raman gauge to 310 GPa. Journal of Applied Physics, 100, 043516–4.
482 483	Badro, J. (2014) Spin Transitions in Mantle Minerals. Annual Review of Earth and Planetary Sciences, 42, 231–248.
484 485 486	Badro, J., Rueff, JP., Vanko, G., Monaco, G., Fiquet, G., and Guyot, F. (2004) Electronic Transitions in Perovskite: Possible Nonconvecting Layers in the Lower Mantle. Science, 305, 383–386.
487 488	Brown, S.P., Thorne, M.S., Miyagi, L., and Rost, S. (2015) A compositional origin to ultralow-velocity zones. Geophysical Research Letters, 2014GL062097.
489 490	Burns, R.G. (1993) Mineralogical Applications of Crystal Field Theory, 563 p. Cambridge University Press.
491 492	Caracas, R. (2010) Spin and structural transitions in AlFeO ₃ and FeAlO ₃ perovskite and post-perovskite. Physics of the Earth and Planetary Interiors.
493 494 495	Catalli, K., Shim, SH., Prakapenka, V.B., Zhao, J., Sturhahn, W., Chow, P., Xiao, Y., Liu, H., Cynn, H., and Evans, W.J. (2010) Spin state of ferric iron in MgSiO ₃ perovskite and its effect on elastic properties. Earth and Planetary Science Letters, 289, 68–75.
496 497 498 499	Catalli, K., Shim, SH., Dera, P., Prakapenka, V.B., Zhao, J., Sturhahn, W., Chow, P., Xiao, Y., Cynn, H., and Evans, W.J. (2011) Effects of the Fe ³⁺ spin transition on the properties of aluminous perovskite—New insights for lower-mantle seismic heterogeneities. Earth and Planetary Science Letters, 310, 293–302.
500 501	Dorfman, S.M., and Duffy, T.S. (2014) Effect of Fe-enrichment on seismic properties of perovskite and post-perovskite in the deep lower mantle. Geophysical Journal

Dorfman, S.M., Shieh, S.R., Meng, Y., Prakapenka, V.B., and Duffy, T.S. (2012) Synthesis and equation of state of perovskites in the (Mg, Fe)₃Al₂Si₃O₁₂ system to 177 GPa. Earth and

505 Planetary Science Letters, 357–358, 194–202.

International, 197, 910-919.

- Dorfman, S.M., Meng, Y., Prakapenka, V.B., and Duffy, T.S. (2013) Effects of Fe-enrichment on the equation of state and stability of (Mg,Fe)SiO₃ perovskite. Earth and Planetary Science Letters, 361, 249–257.
- Dorfman, S.M., Dutton, S.E., Potapkin, V., Chumakov, A., Rueff, J.-P., Chow, P., Xiao, Y.,
 Cava, R.J., Duffy, T.S., McCammon, C.A., and others (2016) Electronic transitions of
 iron in almandine-composition glass to 91 GPa. American Mineralogist, 101.

512 513 514	Dyar, M.D., Agresti, D.G., Schaefer, M.W., Grant, C.A., and Sklute, E.C. (2006) Mössbauer spectroscopy of Earth and planetary materials. Annual Review of Earth and Planetary Sciences, 34, 83–125.
515 516	Fei, Y., Virgo, D., Mysen, B.O., Wang, Y., and Mao, Hk. (1994) Temperature-dependent electron delocalization in (Mg,Fe)SiO3 perovskite. American Mineralogist, 79, 826–837.
517 518 519	Fei, Y., Wang, Y., and Finger, L.W. (1996) Maximum solubility of FeO in (Mg,Fe)SiO ₃ -perovskite as a function of temperature at 26 GPa: Implication for FeO content in the lower mantle. Journal of Geophysical Research, 101, 11525–11530.
520 521 522	Frost, D.J., and Langenhorst, F. (2002) The effect of Al ₂ O ₃ on Fe–Mg partitioning between magnesiowüstite and magnesium silicate perovskite. Earth and Planetary Science Letters, 199, 227–241.
523 524	Frost, D.J., and McCammon, C.A. (2008) The redox state of Earth's mantle. Annual Review of Earth and Planetary Sciences, 36, 389–420.
525 526 527	Frost, D.J., Liebske, C., Langenhorst, F., McCammon, C.A., Trønnes, R.G., and Rubie, D.C. (2004) Experimental evidence for the existence of iron-rich metal in the Earth's lower mantle. Nature, 428, 409–412.
528 529	Grand, S.P. (2002) Mantle Shear–Wave Tomography and the Fate of Subducted Slabs. Philosophical Transactions of the Royal Society of London A, 360, 2475–91.
530 531	Greenwood, N.N., and Gibb, T.C. (1971) Low-spin Iron(II) and Iron(III) Complexes. In Mössbauer Spectroscopy pp. 169–193. Springer Netherlands.
532 533 534	Grüninger, H., Liu, Z., Siegel, R., Ballaran, T.B., Katsura, T., Senker, J., and Frost, D.J. (2019) Oxygen Vacancy Ordering in Aluminous Bridgmanite in the Earth's Lower Mantle. Geophysical Research Letters, 46, 8731–8740.
535 536 537	Gu, C., Catalli, K., Grocholski, B., Gao, L., Alp, E., Chow, P., Xiao, Y., Cynn, H., Evans, W.J., and Shim, SH. (2012) Electronic structure of iron in magnesium silicate glasses at high pressure. Geophysical Research Letters, 39.
538 539 540	Gu, T., Li, M., McCammon, C., and Lee, K.K.M. (2016) Redox-induced lower mantle density contrast and effect on mantle structure and primitive oxygen. Nature Geoscience, 9, 723–727.

Hsu, H., Umemoto, K., Blaha, P., and Wentzcovitch, R.M. (2010) Spin states and hyperfine

interactions of iron in (Mg,Fe)SiO₃ perovskite under pressure. Earth and Planetary

Science Letters, 294, 19–26.

541542

544	Hsu, H., Blał	1a, P.,	, Coco	ccioni, N	1., and	l We	ntzcov	itch,	R.M.	(2011)) Spin	-State	Crosso	ver a	ınd
	T.T.	~	T			~		~ . ~	-						

Hyperfine Interactions of Ferric Iron in MgSiO₃ Perovskite. Physical Review Letters,

546 106, 118501.

- 547 Hu, Q., Kim, D.Y., Yang, W., Yang, L., Meng, Y., Zhang, L., and Mao, H.-K. (2016) FeO₂ and
- FeOOH under deep lower-mantle conditions and Earth's oxygen-hydrogen cycles.
- Nature, 534, 241–244.
- Hummer, D.R., and Fei, Y. (2012) Synthesis and crystal chemistry of Fe3+-bearing
- (Mg,Fe3+)(Si,Fe3+)O3 perovskite. American Mineralogist, 97, 1915–1921.
- Ishii, M., and Tromp, J. (1999) Normal-Mode and Free-Air Gravity Constraints on Lateral
- Variations in Velocity and Density of Earth's Mantle. Science, 285, 1231–1236.
- Ismailova, L., Bykova, E., Bykov, M., Cerantola, V., McCammon, C., Ballaran, T.B., Bobrov,
- A., Sinmyo, R., Dubrovinskaia, N., Glazyrin, K., and others (2016) Stability of Fe, Al-
- bearing bridgmanite in the lower mantle and synthesis of pure Fe-bridgmanite. Science
- 557 Advances, 2, e1600427.
- Jackson, J.M., Sturhahn, W., Shen, G., Zhao, J., Hu, M.Y., Errandonea, D., Bass, J.D., and Fei,
- Y. (2005) A synchrotron Mössbauer spectroscopy study of (Mg,Fe)SiO₃ perovskite up to
- 560 120 GPa. American Mineralogist, 90, 199–205.
- Keppler, H., Dubrovinsky, L.S., Narygina, O., and Kantor, I. (2008) Optical Absorption and
- Radiative Thermal Conductivity of Silicate Perovskite to 125 Gigapascals. Science, 322,
- 563 1529–1532.
- Kupenko, I., McCammon, C.A., Sinmyo, R., Cerantola, V., Potapkin, V., Chumakov, A.I.,
- Kantor, A.P., Rüffer, R., and Dubrovinsky, L.S. (2015) Oxidation state of the lower
- mantle: In situ observations of the iron electronic configuration in bridgmanite at extreme
- conditions. Earth and Planetary Science Letters, 423, 78–86.
- Lau, H.C.P., Mitrovica, J.X., Davis, J.L., Tromp, J., Yang, H.-Y., and Al-Attar, D. (2017) Tidal
- tomography constrains Earth's deep-mantle buoyancy. Nature, 551, 321–326.
- Lin, J.-F., Speziale, S., Mao, Z., and Marquardt, H. (2013) Effects of the electronic spin
- transitions of iron in lower mantle minerals: Implications for deep mantle geophysics and
- geochemistry. Reviews of Geophysics, 51.
- Liu, J., Li, J., Hrubiak, R., and Smith, J.S. (2016) Origins of ultralow velocity zones through
- slab-derived metallic melt. Proceedings of the National Academy of Sciences, 113, 5547–
- 575 5551.
- Liu, J., Hu, Q., Kim, D.Y., Wu, Z., Wang, W., Xiao, Y., Chow, P., Meng, Y., Prakapenka, V.B.,
- Mao, H.-K., and others (2017) Hydrogen-bearing iron peroxide and the origin of
- 578 ultralow-velocity zones. Nature, 551, 494.

579	Liu, J., Dorfman, S.M., Zhu, F., Li, J., Wang, Y., Zhang, D., Xiao, Y., Bi, W., and Alp, E.E
580	(2018) Valence and spin states of iron are invisible in Earth's lower mantle. Nature

Communications, 9, 1284.

- Liu, Z., Boffa Ballaran, T., Huang, R., Frost, D.J., and Katsura, T. (2019) Strong correlation of oxygen vacancies in bridgmanite with Mg/Si ratio. Earth and Planetary Science Letters, 523, 115697.
- Lobanov, S.S., Holtgrewe, N., Lin, J.-F., and Goncharov, A.F. (2017) Radiative conductivity and abundance of post-perovskite in the lowermost mantle. Earth and Planetary Science Letters, 479, 43–49.
- Long, Y.W., Hayashi, N., Saito, T., Azuma, M., Muranaka, S., and Shimakawa, Y. (2009)
 Temperature-induced A-B intersite charge transfer in an A-site-ordered LaCu3Fe4O12
 perovskite. Nature, 458, 60-63.
- Mao, H. -k., Xu, J., and Bell, P.M. (1986) Calibration of the Ruby Pressure Gauge to 800 kbar Under Quasi-Hydrostatic Conditions. Journal of Geophysical Research, 91, 4673–4676.
- Mao, W.L., Mao, H., Sturhahn, W., Zhao, J., Prakapenka, V.B., Meng, Y., Shu, J., Fei, Y., and Hemley, R.J. (2006) Iron-rich post-perovskite and the origin of ultralow-velocity zones. Science, 312, 564–565.
- Mao, Z., Lin, J.-F., Yang, J., Inoue, T., and Prakapenka, V.B. (2015) Effects of the Fe3+ spin transition on the equation of state of bridgmanite. Geophysical Research Letters, 42,
 2015GL064400.
- Mattson, S.M., and Rossman, G.R. (1987) Identifying characteristics of charge transfer transitions in minerals. Physics and Chemistry of Minerals, 14, 94–99.
- McCammon, C., Glazyrin, K., Kantor, A., Kantor, I., Kupenko, I., Narygina, O., Potapkin, V., Prescher, C., Sinmyo, R., Chumakov, A., and others (2013) Iron spin state in silicate perovskite at conditions of the Earth's deep interior. High Pressure Research, 0, 1–10.
- Pasternak, M.P., Xu, W.M., Rozenberg, G.Kh., and Taylor, R.D. (2002) Electronic, Magnetic and Structural Properties of the RFeO₃ Antiferromagnetic-Perovskites at Very High Pressures. In Symposium D Perovskite Materials Vol. 718.
- Piet, H., Badro, J., Nabiei, F., Dennenwaldt, T., Shim, S.-H., Cantoni, M., Hébert, C., and Gillet,
 P. (2016) Spin and valence dependence of iron partitioning in Earth's deep mantle.
 Proceedings of the National Academy of Sciences, 201605290.
- Potapkin, V., Chumakov, A.I., Smirnov, G.V., Celse, J.-P., Rüffer, R., McCammon, C., and
 Dubrovinsky, L. (2012) The ⁵⁷Fe Synchrotron Mössbauer Source at the ESRF. Journal of
 Synchrotron Radiation, 19, 559–569.

613	Potapkin, V., McCammon, C.A., Glazyrin, K.D., Kantor, A.P., Kupenko, I., Prescher, C.,
614	Sinmyo, R., Smirnov, G.V., Chumakov, A.I., Rüffer, R., and others (2013) Effect of iron
615	oxidation state on the electrical conductivity of the Earth's lower mantle. Nature
616	Communications, 4, 1427.
617	Prescher, C., McCammon, C., and Dubrovinsky, L. (2012) MossA: a program for analyzing
618	energy-domain Mössbauer spectra from conventional and synchrotron sources. Journal of
619	Applied Crystallography, 45, 329–331.
620	Prescher, C., Weigel, C., McCammon, C.A., Narygina, O., Potapkin, V., Kupenko, I., Sinmyo,
621	R., Chumakov, A.I., and Dubrovinsky, L.S. (2014) Iron spin state in silicate glass at high
622	pressure: Implications for melts in the Earth's lower mantle. Earth and Planetary Science
623	Letters, 385, 130–136.
624	Ricolleau, A., Fei, Y., Cottrell, E., Watson, H., Deng, L., Zhang, L., Fiquet, G., Auzende, AL.,
625	Roskosz, M., Morard, G., and others (2009) Density profile of pyrolite under the lower
626	mantle conditions. Geophysical Research Letters, 36, L06302.
627	Rivers, M., Prakapenka, V., Kubo, A., Pullins, C., Holl, C.M., and Jacobsen, S.D. (2008) The
628	COMPRES/GSECARS gas-loading system for diamond anvil cells at the Advanced
629	Photon Source. High Pressure Research, 28, 273–292.
630	Rost, S., Garnero, E.J., Williams, Q., and Manga, M. (2005) Seismological constraints on a
631	possible plume root at the core-mantle boundary. Nature, 435, 666–669.
632	Rüffer, R., and Chumakov, A.I. (1996) Nuclear Resonance Beamline at ESRF. Hyperfine
633	Interactions, 97–98, 589–604.
634	Shim, SH., Grocholski, B., Ye, Y., Alp, E.E., Xu, S., Morgan, D., Meng, Y., and Prakapenka,
635	V.B. (2017) Stability of ferrous-iron-rich bridgmanite under reducing midmantle
636	conditions. Proceedings of the National Academy of Sciences, 201614036.
637	Shukla, G., Cococcioni, M., and Wentzcovitch, R.M. (2016) Thermoelasticity of Fe3+- and Al-
638	bearing bridgmanite: Effects of iron spin crossover. Geophysical Research Letters, 43,
639	5661–5670.
640	Sinmyo, R., Pesce, G., Greenberg, E., McCammon, C., and Dubrovinsky, L. (2014) Lower
641	mantle electrical conductivity based on measurements of Al, Fe-bearing perovskite under
642	lower mantle conditions. Earth and Planetary Science Letters, 393, 165–172.
643	Tange, Y., Takahashi, E., Nishihara, Y., Funakoshi, K., and Sata, N. (2009) Phase relations in

the system MgO-FeO-SiO₂ to 50 GPa and 2000°C: An application of experimental

techniques using multianvil apparatus with sintered diamond anvils. Journal of

Geophysical Research, 114, B02214.

643

644

647 648 649	perovskite and the post-perovskite phase transition. Physics of the Earth and Planetary Interiors, 160, 319–325.
650 651	Weber, J.K.R., Hampton, D.S., Merkley, D.R., Rey, C.A., Zatarski, M.M., and Nordine, P.C. (1994) Aero-acoustic levitation: A method for containerless liquid-phase processing at
652	high temperatures. Review of Scientific Instruments, 65, 456–465.
653	Wicks, J.K., Jackson, J.M., and Sturhahn, W. (2010) Very low sound velocities in iron-rich
654	(Mg,Fe)O: Implications for the core-mantle boundary region. Geophysical Research
655	Letters, 37, 5 PP.
656	Williams, Q., and Garnero, E.J. (1996) Seismic Evidence for Partial Melt at the Base of Earth's
657	Mantle. Science, 273, 1528–1530.
658	Xu, Y., and McCammon, C.A. (2002) Evidence for ionic conductivity in lower mantle
659	(Mg,Fe)(Si,Al)O 3 perovskite. Journal of Geophysical Research, 107.
660	